ANL-79-33

DR 160

ANL-79-33

296
10/15/79

MASTER

BIAXIAL CREEP-FATIGUE BEHAVIOR OF TYPE 316H STAINLESS STEEL TUBE

by

S. Majumdar

ARGONNE NATIONAL LABORATORY, ARGONNE, ILLINOIS

Prepared for the U. S. DEPARTMENT OF ENERGY
under Contract W-31-109-Eng-38

DISCLAIMER

Printed in the United States of America
Available from
National Technical Information Service
U. S. Department of Commerce
5285 Port Royal Road
Springfield, VA 22161

NTIS price codes
Printed copy: A03
Microfiche copy: A01

Distribution Category:
Solar Thermal—Large Scale Systems
(UC-62c)

ANL-79-33

ARGONNE NATIONAL LABORATORY
9700 South Cass Avenue
Argonne, Illinois 60439

BIAXIAL CREEP-FATIGUE BEHAVIOR OF TYPE 316H STAINLESS STEEL TUBE

by

S. Majumdar

Materials Science Division

April 1979

THIS PAGE

WAS INTENTIONALLY

LEFT BLANK

TABLE OF CONTENTS

LIST OF FIGURES

LIST OF FIGURES (CONTD.)

LIST OF TABLES

BIAXIAL CREEP-FATIGUE BEHAVIOR OF TYPE 316H STAINLESS STEEL TUBE

by

S. Majumdar

ABSTRACT

Biaxial creep-fatigue test data for Type 316 stainless steel tubes at 1100°F are presented. The specimens were subjected to constant internal pressure and fluctuating axial strain with and without hold times in tension as well as compression. The results show that internal pressure significantly affects diametral ratchetting and axial stress range. Axial tensile hold is found to be more damaging than axial compressive hold even under a biaxial state of stress.

NOMENCLATURE

E	Young's modulus
$\Delta\sigma$	Axial stress range
$\Delta\varepsilon_{tot}$	Axial total strain range
$\Delta\varepsilon_{pl}$	Axial plastic strain range
σ_{t_o}	Axial stress at the beginning of tensile hold time
σ_{c_o}	Axial stress at the beginning of compressive hold time
σ_{t_R}	Relaxed axial stress at the end of tensile hold time
σ_{t_C}	Relaxed axial stress at the end of compressive hold time
σ_a	Axial stress
σ_θ	Hoop stress
p	Internal pressure

I. INTRODUCTION

The highly cyclic nature of solar central receiver operating conditions is likely to create difficult structural design problems. Solar plants will undergo at least one major start-up and shutdown cycle per day, with the likelihood that additional thermal cycles will be imposed by intermittent cloud cover and unscheduled maintenance and repair. Thus, critical elevated-temperature components may be expected to accumulate on the order of tens of thousands of thermal and associated strain cycles over a 30-year design life. In addition, repeated thermal cycling of superheater or boiler tubing while under internal pressure can lead to incremental growth of the diameter or ratchetting. The analyst must therefore design against structural failure caused by thermal fatigue, creep-fatigue interaction and excessive deformation caused by ratchetting.

Another aspect of solar-plant operating conditions likely to cause design difficulties is that, during steady-state operation, the boiler and superheater tubing will be loaded nonaxisymmetrically at elevated temperatures.[1,2] In particular, the boiler or the critical passes of the superheater tubing will be loaded during daytime operation such that the outer tubing wall on the high-temperature side will experience a large compressive axial stress and a moderate compressive hoop stress. On the other hand, the inner wall on the high-temperature side will be subjected to a moderate compressive axial stress and a small tensile hoop stress. Considerable information on constitutive relations under compressive and mixed tensile-plus-compressive creep conditions will be required to permit structural analyses of the components. In addition, failure criteria for multiaxial tensile-plus-compressive creep-fatigue conditions must be developed.

Elevated-temperature design rules applicable to solar-power-plant boilers and piping are set forth in Section I of the ASME Boiler and Pressure Vessel Code. However, Section I was not developed with the highly cyclic and often complex loading conditions of solar power-plant components in mind, and no specific design rules for treating fatigue, creep-fatigue, or ratchetting are provided. Applicable design rules from the nuclear portions of the Code (Section III and Case N47) are likely to result in excessively conservative designs. For example, Case N47 would consider the compressive hold time on the hot side of the superheater tubing to be as damaging as an equal tensile hold time, although available data [3] indicate that this is not the case for many materials, at least for uniaxial loadings.

Current design procedure for the solar-plant-boiler superheater tubing is to perform a creep-fatigue analysis using elevated-temperature nuclear rules (Case N47) but to ignore creep damage caused by compressive stresses. Thus, hold times under compressive stresses are assumed to be nondamaging. As stated above, this assumption appears to be reasonable for austenitic stainless steels under uniaxial loading conditions, but it has never been verified for biaxial loading situations, particularly where the stress is tensile in one direction and compressive in the other. Furthermore, virtually no creep-fatigue data exist for Type 316H stainless steel, which is one of the candidate materials for solar application, even under uniaxial loading conditions.

Under the present program, biaxial creep-fatigue tests (constant tensile hoop stress and cyclic axial strain with hold times in tension or compression) have been performed on Type 316H stainless steel superheater tubing material. Times to failure have been shortened by increasing the magnitude of the axial strain range, and by using a considerably shorter hold time, than that expected in service. Details of experiments, results obtained and their discussion are contained in the following sections.

II. EXPERIMENTAL DETAILS

A. Material

Type 316H stainless steel (Heat No. 180124) used in this work was procured from Pacific Tube Co. of Los Angeles, California in the form of 1-in.-OD x 0.109-in. min. wall seamless tubing. Chemical analysis of the material, which satisfied ASME specification SA-213, as supplied by the vendor is shown in Table I. The nominal room-temperature mechanical properties of the material as supplied by the vendor are shown in Table II. Micrographs of the as-received material, shown in Fig. 1, indicate that the grain structure is generally equiaxed with average grain sizes 32.6 μ (ASTM 6.5) in transverse section and 33.5 μ (ASTM 6.4) in longitudinal section.

B. Specimen Fabrication

The 1-in.-diameter seamless tubing, which was supplied by the vendor in 17-ft lengths, was cut into 12-in. sections. Some of these were machined to the dimensions shown in Fig. 2a to provide the straight gauge section specimens. The wall thickness at the gauge section was nominally 0.077 in. The wall thicknesses at the center of two of these specimens were reduced by 0.005 and 0.010 in., respectively, by hand polishing. In the latter half of the program, hourglass-shaped specimens were used in order to restrict the failure location to the center of the specimens. These were machined from the remaining 12-in. tube sections as shown in Fig. 2b. A large radius of 9-1/8 in. was used in the hourglassing to minimize stress-concentration effects ($K_t \approx 1.01$). The adequacy of this choice was verified by the test results. Each specimen was polished mechanically at the central gauge section to give a finish of better than 8 microinches on both the inner and outer surfaces.

C. Heat Treatment

All the specimens were tested in the as-received condition without any annealing or preaging treatment.

D. Test Equipment and Procedure

The biaxial fatigue testing was carried out in a closed-loop servo-controlled MTS testing machine (Fig. 3) using constant internal pressure and axial strain control. The internal pressure was provided by a commercially available pressurized nitrogen bottle. The axial strain in the

specimens was measured by a high-temperature axial extensometer with a 1/2-in. gauge length, and the diametral strain was measured by a high-temperature diametral extensometer. The axial load was measured by a 40-kip load cell placed in series with the specimen. The specimen was heated by a Lepel induction heater operating at a frequency of 455 kHz. Figure 4 shows a close-up view of a specimen inside the induction heating coil with the axial and diametral extensometers in position.

In order to determine the temperature distribution in the test specimens a total of 44 thermocouples (11 along each of four azimuthal planes) were distributed axially along the specimen at 1/4-in. intervals (Fig. 5). Figure 6 shows typical temperature profiles in a straight-gauge specimen at 0, 1100 and 2000 psi internal pressure. Figure 7 shows similar plots for the hourglass specimen. Note that the temperature profiles are dependent upon the internal pressure and the specimen geometry. However, for a given specimen geometry at a fixed internal pressure the temperature profile was reproducible to within $\pm 5°F$. The dip in the center of the temperature profile is caused by the heat carried away by the extensometers, which act as heat sinks. The maximum temperature variation over the central 1/2 in. of the gauge section was about 20°F for both the hourglass and straight-gauge specimens. In an actual test the temperature in the specimen was regulated by a control thermocouple spot welded at a distance of 1-1/4 in. from the center for the straight-gauge specimen and 1 in. for the hourglass specimen. Eight other thermocouples were attached to the specimen, four at the top and four at the bottom, distributed symmetrically about the center and at the same distance from it as the control thermocouple. The set point in the Lepel heater was then adjusted so that the average reading of these thermocouples corresponded to the desired temperature in the central 1/2 in. of the specimen as determined from the calibrated specimen. Although the specimen wall is thinnest in the central region, several specimens failed outside this region, at one of the thermocouple locations.

Since the specimen grip was of the split-collar clamping-ring type, special care was taken in aligning the specimen while the clamping-ring bolts were tightened. Four strain gauges were attached at 90° intervals around the circumference near the bottom end of the specimen. The bottom end of the specimen was first gripped and the clamping-ring bolts were tightened sequentially while maintaining alignment at the top end by a mechanical gauge. The readings on the strain gauges were noted, and the top end of the specimen was then gripped and the clamping-ring bolts tightened sequentially to minimize bending. The specimen was then axially loaded in both tension and compression in the elastic range to ensure that no bending occurred as indicated by the strain gauges. Good alignment of the specimen was further evidenced by initiation of multiple cracks around the circumferences of many fractured specimens.

The test procedure consisted of first heating the specimen to the desired temperature with zero axial load, and holding the temperature steady until the whole system came to thermal equilibrium. The internal pressure, if any, was then applied and the specimen was kept at the temperature for sufficient time to allow the new temperature distribution to come to equilibrium. The specimen was then cycled axially under axial strain control.

Hysteresis loops of axial stress versus axial strain and axial strain versus diametral strain were recorded on x-y plotters at regular intervals. Each individual signal was also plotted on a strip-chart recorder. For the internally pressurized specimens, the test was shut down automatically when a crack penetrated through the wall. For the unpressurized specimens, the test was shut down automatically when the specimen fractured. The number of cycles to failure was determined from the diametral-strain strip-chart recording at the onset of rapid change in the diametral strain. No attempt was made to measure crack lengths in the specimens. Some of the fracture surfaces of the specimens were studied using scanning electron microscopy.

E. Test Matrix

All testing was carried out at a total strain range of 0.5% and at a nominal temperature of 1100°F. Tests were carried out with 0, 1100, and 2000 psi constant internal pressure and with 0, 1-minute tensile and 1-minute compressive hold times (at the maximum axial strain limit). A total of 16 tests were conducted. The first 10 were on straight-gauge specimens. Since some of these specimens failed outside the axial extensometer gauge length, the latter 6 tests were conducted with the hourglass specimens; this alleviated the problem. A description of the test matrix is given in Table III.

III. EXPERIMENTAL DATA

A summary of all the biaxial fatigue tests conducted on Type 316 stainless steel tubes is shown in Table IV where the reported plastic strain range, diametral strain range and axial stress range are measured at approximately the half life of each test. The temperatures reported in the third column are the calculated average temperatures at the gauge section. The axial plastic strain ranges ($\Delta\varepsilon_{pl}$) reported were computed from the measured axial total strain ranges ($\Delta\varepsilon_{tot}$) and the axial stress ranges ($\Delta\sigma$) by the equation

$$\Delta\varepsilon_{pl} = \Delta\varepsilon_{tot} - \frac{\Delta\sigma}{E} ,$$

where

$$E = 22.2 \times 10^{6} \text{ psi} .$$

The hoop-stress values reported were computed by the thin-wall tube-approximation formula using the average radius of the tube. The diametral strains reported are the calculated hoop strains at the outside-diameter surface, obtained by dividing the measured diametral displacements by the outside diameter of the tube at the gauge section.

Traces of the axial stress-axial strain hysteresis loops at cycles 1, 10, and the approximate half life for all the tests are given in Figs. 8 to

23. The axial stresses on these plots have not been corrected for the component due to internal pressure. The corrections are about +2.5 and +4.6 ksi for the 1100- and 2000-psi internal-pressure cases, respectively. However, the axial stresses reported in Table IV include the corrections due to internal pressure.

The stress-relaxation data for all the hold-time tests are included in Table V: σ_{t_o} and σ_{c_o} represent stresses at the beginning of the tensile and compressive hold time, respectively, and σ_{t_R} and σ_{c_R} represent the relaxed stresses at the end of the tensile and compressive hold time, respectively.

IV. DISCUSSION OF RESULTS

An examination of Table IV shows that the stress-strain data for the hourglass and straight-gauge specimens are similar; the same is true of the failure data. However, the likelihood of the specimen failing outside the axial extensometer tips is much smaller for the hourglass specimens than for the straight-gauge specimens. The axial stress hardening with cycles for three continuous-cycling tests is shown in Fig. 24. Note that the straight-gauge and hourglass specimens show similar hardening behavior. The slightly smaller stress range for the hourglass specimens could be the result of the fact that they were tested at an ∿40-50°F higher temperature than the straight-gauge specimens. A comparison of the hysteresis loops at half life for the two types of specimens subjected to 1-min tensile-hold loading is shown in Fig. 25. Although the straight-gauge specimens show slightly larger stress ranges than the hourglass specimens, they are considered to be within the same scatter band. A comparison of the ratchetting behavior of the hourglass and straight-gauge specimens is shown in Fig. 26. Note that the two types of specimens behave similarly even though the tensile-hold specimens ratchet more than the compressive-hold specimens in the early part of the tests. In all cases, however, the hourglass specimens tend to ratchet more than the straight-gauge specimens for the first few cycles. This could be the results of the slight stress concentration that occurs in the hourglass specimens.

The stress-relaxation behavior is similar for the two types of specimens (Table V). However, the hourglass specimens consistently tend to have a slightly lower stress than the straight-gauge specimens. The amount of axial stress relaxation seems to be independent of specimen type and internal pressure. Typical stress-relaxation behavior for a one-minute compressive-hold test is shown in Fig. 27. Note that in spite of considerable hardening as the number of cycles increases, the amount of stress relaxation per cycle is approximately constant. The rapid drop in the stress at the beginning of the hold time occurs for two reasons. First, the load drop is a result of the anelastic effect caused by the sudden change in the applied strain rate. Secondly, because of the inertia of the test system, strain in the specimen slightly exceeds the strain limits before going into the hold-time mode.

The rapid load drop is thus partially a result of the attempt by the closed-loop system to correct for the slight overshoot in strain.

The effect of internal pressure on the axial stress hardening is shown in Fig. 28. The specimens with higher internal pressure tend to have a higher rate of hardening as well as a larger half-life stress range. This may be due to the larger diametral ratchetting experienced by the specimen with larger internal pressure. Tests without diametral ratchetting (i.e., with both internal and external pressure) are necessary to determine whether this hardening is truly a biaxial stress effect or whether it is a consequence of the mean plastic strain that accumulates as a result of ratchetting. Another interesting feature of Fig. 28 is that the specimens without hold time reach a stable stress range with cycling whereas the specimens with either tensile or compressive hold time continue to harden to the end of the test without ever really attaining a stable stress-range value.

The effect of internal pressure on the ratchetting behavior of the tubes under continuous cycling is shown in Fig. 29. As expected, the higher the internal pressure, the larger the diametral ratchetting. Note that although tests 1001, 1012 and 1044 were each tested with an internal pressure of 1100 psi, test 1044 had about 50% more ratchetting than the other two. The reason for this can be traced to the temperature of specimen 1044, which was about 50°F hotter than the other two (see Table IV). Similarly, test 1031 showed more ratchetting than test 1059 under an internal pressure of 2000 psi because the latter specimen was about 30°F cooler than the former. This strong dependence of ratchetting on temperature suggests that the majority of the ratchetting strain is due to thermally activated creep. It is interesting to note that if one analyzed these specimens on the assumption that creep is negligible because no hold time is involved in the cycle, one would grossly underestimate the diametral ratchetting strain. In fact, a rate-independent plasticity analysis of the tube would show a saturation in ratchetting strain after accumulation of a much smaller amount of diametral plastic strain than is observed in the tests.[4] This points out the importance of including creep effects during transient loadings in a ratchetting analysis. However, it is expected that as the hold time increases, the contribution of thermal creep to the ratchetting will become more significant during hold times than during the transients. It is interesting to plot the diametral ratchetting as a function of the number of cycles as well as with time for tests with and without hold times. Such plots are shown in Figs. 30 and 31. Note that the specimens subjected to continuous cycling ratchet faster than the ones subjected to hold time when the data are plotted against time. However, the reverse might be true when the data are plotted against cycles.

Another interesting observation can be made regarding the hysteresis loop shape for the tests with hold times. Although the tension going and the compression going halves of the hysteresis loop were similar in shape for the first few hundred cycles, this is not the case when the specimen has hardened significantly. Representative hysteresis loops are shown for the 1-min tensile-hold and 1-min compressive-hold tests in Fig. 32. Note that the tension going half of the hysteresis loop of the tensile-hold test and

the compression going half of the hysteresis loop of the compressive-hold test are almost bilinear in shape, whereas the remaining halves of the hysteresis loops are rounded as usual. Such behavior was not observed for the continuous-cycling tests. The reason for this is not fully understood but is suspected to be related to the asymmetry in the dislocation structure created by the unsymmetric hold time.

The fracture surfaces of some of the specimens were examined by scanning electron microscopy. A number of failed specimens displayed evidence of multiple crack initiation around the circumference of the tube, indicating that specimen alignment was adequate. It was found that under continuous cycling and with 1-min compressive hold time with or without internal pressure, the specimens failed transgranularly with striations appearing on the fracture surface (Figs. 33 and 34). However, for the 1-min tensile-hold test the fracture was predominantly intergranular, as shown in Fig. 35. In most cases the crack(s) initiated from the inner-diameter surface and propagated outwards.

V. CONCLUSIONS AND RECOMMENDATIONS

The hourglass type of specimen is preferable to the straight-gauge type for conducting biaxial fatigue testing. The two types of specimens are similar with respect to both stress-strain response and ratchetting behavior.

Type 316H stainless steel (as received) hardens cyclically; both the rate of hardening and the stable axial stress range increase with increasing internal pressure. It is not clear whether this difference in hardening behavior is due to the biaxiality of the stress field or to the larger diametral ratchetting in the specimens associated with larger internal pressure. Tests with both internal and external pressures (to prevent ratchetting) are needed to determine whether this behavior is truly due to the biaxiality of the stress field or not.

The effect of internal pressure (up to 2000 psi) on the continuous-cycling and 1-min compressive-hold fatigue life at 1100°F is small. However, it must be remembered that the biaxiality of the stress field (σ_θ/σ_a) in these tests was small. Future testing should concentrate on lower axial strain ranges so that the biaxiality of the stress field is more significant.

The 1-min axial tensile hold is more damaging than the 1-min axial compressive hold for this material at 1100°F even under a biaxial state of stress. This is also borne out by microstructural observation of the fracture surface. The compressive-hold tests fail transgranularly, whereas the tensile-hold tests fail intergranularly.

Although tensile hold is more damaging than compressive hold for this material, the damage during compressive hold is not zero. Tests with longer hold time in compression together with larger biaxiality in the stress field are needed to simulate more closely the type of loading expected in a central solar receiver tube.

ACKNOWLEDGMENTS

The author would like to thank Michael Gorman for conducting the tests and reducing much of the test data and Don Busch for his help in the SEM work. Thanks are also due to Bill Burke for his constant help in running the tests. The author would also like to express his gratitude to Bill Moore of Sandia Laboratories, Livermore, for his support and encouragement.

REFERENCES

1. Central Receiver Solar Thermal Power System, Phase 1, Pilot Plant Preliminary Design Report, Vol. IV, Receiver Subsystem, McDonnell Douglas Astronautics Company Report MDC G6776, May 1977.

2. Central Receiver Solar Thermal Power System, Phase 1, Progress Report for Period Ending December 31, 1975, prepared by Martin Marietta Corporation for the Energy Research and Development Administration, Division of Solar Energy, SAN/1110-76/T1, April 1976.

3. J. B. Conway, R. H. Stentz and J. T. Berling, Fatigue, Tensile and Relaxation Behavior of Stainless Steels, USAEC, TID-26135, 1975.

4. Gopal Gupta, Foster Wheeler Development Corporation, Livingston, New Jersey, personal communication (1978).

Table I. Chemistry of Type 316H Stainless Steel Tubing (Heat 180124)

Element	Content, wt. %	
	Ladle Analysis	Check Analysis
C	0.05	0.06
Mn	1.62	1.64
P	0.024	0.022
S	0.012	0.012
Si	0.60	0.60
Ni	11.96	11.87
Cr	17.00	16.91
Mo	2.26	2.22

Table II. Nominal Room-temperature Mechanical Properties of Type 316H Stainless Steel Tubing (Heat 180124)

Ultimate Strength, ksi	Yield Strength, ksi	% Elongation	Rockwell Hardness	Grain Size
85.25	46.33	65	76-80	ASTM #6

Table III. Test Matrix[a]

Internal Pressure, psi	Hold Time[b], min	Specimen Type	No. of Specimens
0	0	Straight-gauge	2
1100	0	Straight-gauge	2
		Hourglass	1
2000	0	Straight-gauge	1
		Hourglass	1
0	1C	Straight-gauge	2
		Hourglass	1
1100	1C	Straight-gauge	2
		Hourglass	1
1100	1T	Straight-gauge	1
		Hourglass	1
2000	1C	Hourglass	1

[a]Nominal Temperature = 1100°F.
Total Axial Strain Range = 0.5%.
Total Axial Strain Rate = 4×10^{-3}/s.

[b]T and C denote tensile and compressive hold, respectively.

Table IV. Summary of Biaxial Fatigue Data for Type 316H Stainless Steel

Test No.	Specimen Type	Temp., °F	Hold Time[a], min	Internal Pressure, psi	Axial Strain Range, %		Diametral Strain Range, %	Axial Stress, ksi		Average Hoop Stress, ksi	Cycles to Failure	Mean Diametral Strain at Failure, %
					Total	Plastic		Range	Mean			
997	Str. gauge	1065	0	0	0.51	0.19	0.20	71.5	+0.1	0	14156	-0.02
999	Str. gauge	1069	0	0	0.50	0.19	0.19	70.1	+0.0	0	8110	-0.02
1027	Str. gauge	1144	1C	0	0.50	0.16	0.21	74.8	+0.6	0	4047[b]	-0.08
1035	Str. gauge[c]	1100	1C	0	0.49	0.15	0.21	75.1	+1.1	0	9750[d]	-0.06
1052	Hourglass	1100	1C	0	0.50	0.17	0.19	74.0	+1.7	0	13518	-0.10
1001	Str. gauge	1054	0	1100	0.50	0.17	0.19	74.3	+0.7	6.1	15566	+1.05
1012	Str. gauge	1070	0	1100	0.50	0.17	0.20	72.3	+0.8	6.1	9229	+0.96
1044	Hourglass	1110	0	1100	0.50	0.18	0.20	71.3	-0.4	6.1	13474	+1.61
1024	Str. gauge	1132	1C	1100	0.50	0.15	0.18	78.2	+1.2	6.1	5069[e]	+1.18
1033	Str. gauge	1123	1C	1100	0.50	0.14	0.18	78.8	+1.5	6.1	4538[d]	+0.83
1049	Hourglass	1100	1C	1100	0.50	0.16	0.20	75.9	+1.9	6.1	8283	+1.98
1038	Str. gauge[f]	1100	1T	1100	0.50	0.15	0.17	76.8	+0.1	6.1	3821	+1.21
1041	Hourglass	1125	1T	1100	0.50	0.16	0.18	74.8	+0.2	6.1	2746	+1.04
1031	Str. gauge	1128	0	2000	0.50	0.15	0.17	77.6	+0.2	11.0	6739[d]	+2.5
1059	Hourglass	1100	0	2000	0.50	0.15	0.19	77.4	-0.1	11.0	14583[e]	+3.15
1050	Hourglass	1100	1C	2000	0.50	0.12	0.20	84.2	+1.6	11.0	7140[d]	+4.67

[a] T and C denote tensile and compressive hold, respectively.

[b] Specimen overstrained due to power interruption.

[c] Specimen wall thickness reduced by 0.005 in. at center by polishing.

[d] Specimen failed outside gauge section.

[e] Specimen failed at thermocouple.

[f] Specimen wall thickness reduced by 0.01 in. at center by polishing.

Table V. Summary of Relaxation Stresses for the One-minute Hold-time tests on Type 316 Stainless Steel

Test No.	Specimen Type	Temp., °F	Hold Time, min	Internal Pressure, psi	Tensile Stress, ksi		Compressive Stress, ksi	
					σ_{t_o}	σ_{t_b}	σ_{c_o}	σ_{c_R}
1027	Straight-gauge	1144	1C	0	38.0	-	36.8	34.7
1035	Straight-gauge	1100	1C	0	38.7	-	36.4	34.6
1052	Hourglass	1100	1C	0	38.7	-	35.3	32.7
1024	Straight-gauge	1132	1C	1100	40.3	-	37.9	35.7
1033	Straight-gauge	1123	1C	1100	40.9	-	37.9	35.2
1049	Hourglass	1100	1C	1100	39.9	-	36.0	33.6
1050	Hourglass	1100	1C	2000	43.7	-	40.5	37.8
1038	Straight-gauge	1100	1T	1100	38.5	35.9	38.3	-
1041	Hourglass	1125	1T	1100	37.6	35.1	37.2	-

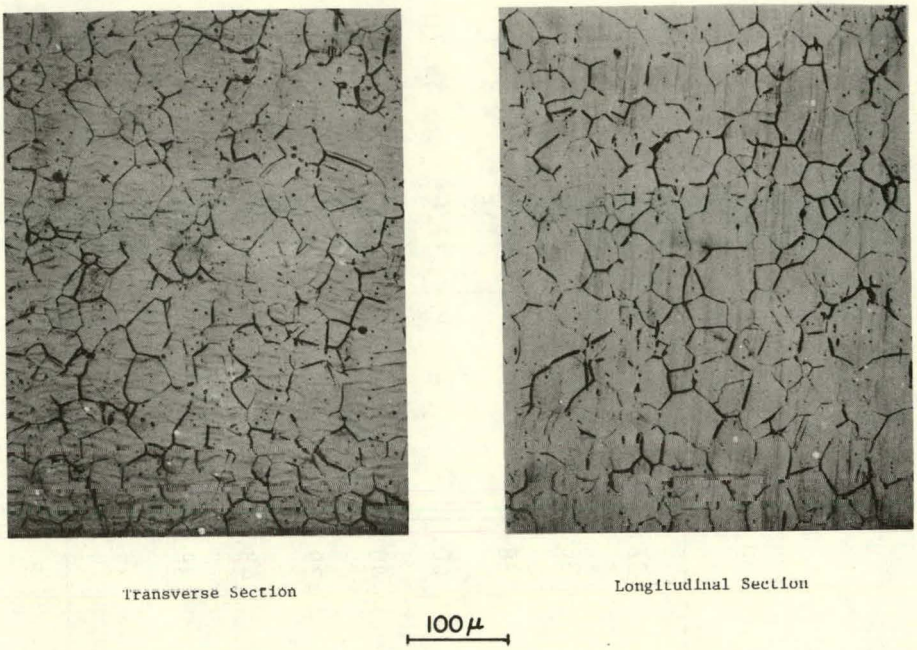

Fig. 1. Typical Microstructure of As-received Type 316H Stainless Steel. Neg. No. MSD-66265.

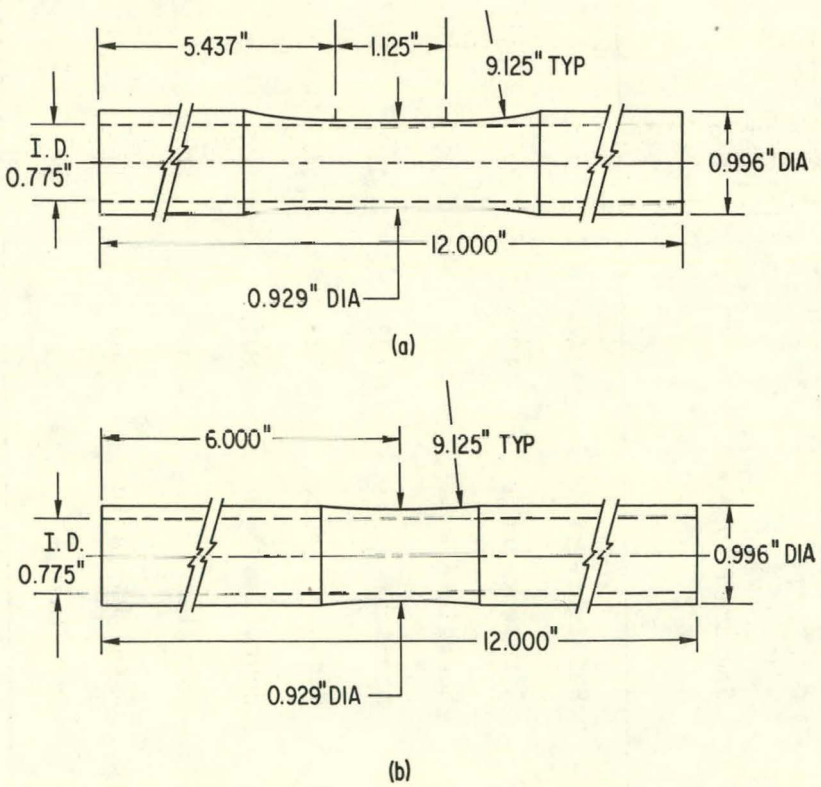

Fig. 2. Specimen Geometry. (a) Straight gauge; (b) hourglass. Neg. No. MSD-66258.

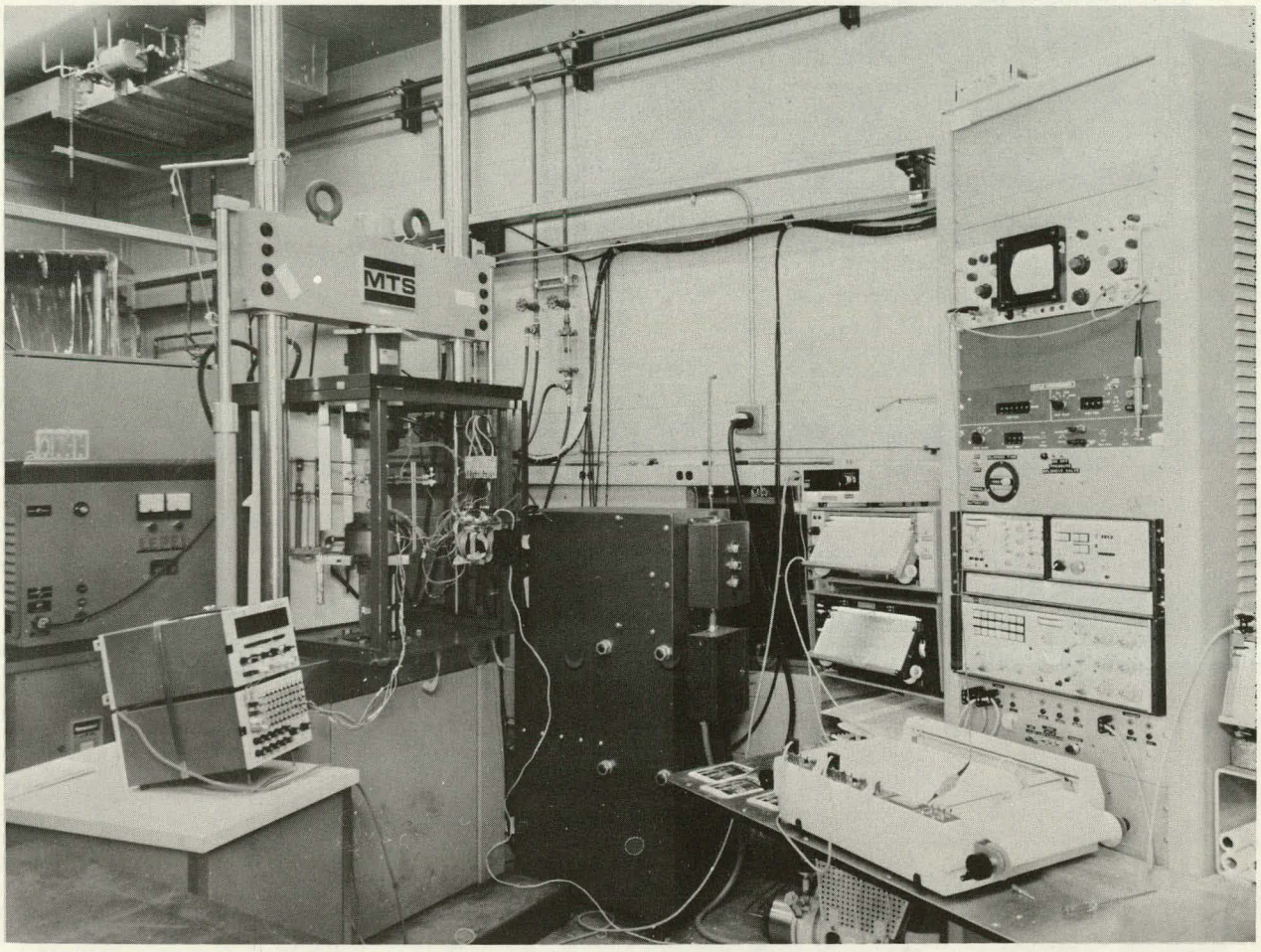

Fig. 3. Typical Test Setup.

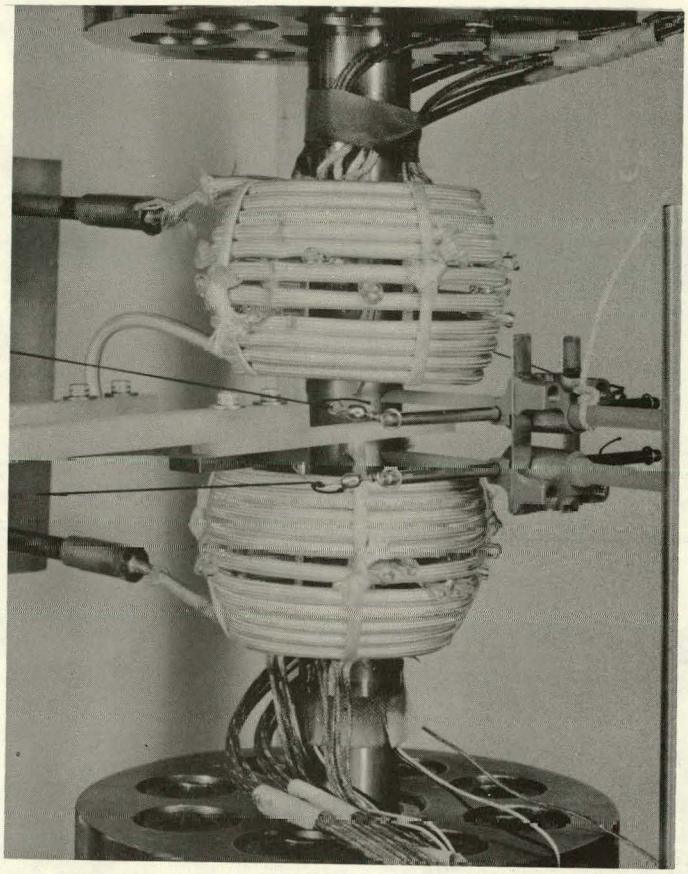

Fig. 4

Close-up View of the Bi-axial Fatigue Specimen.

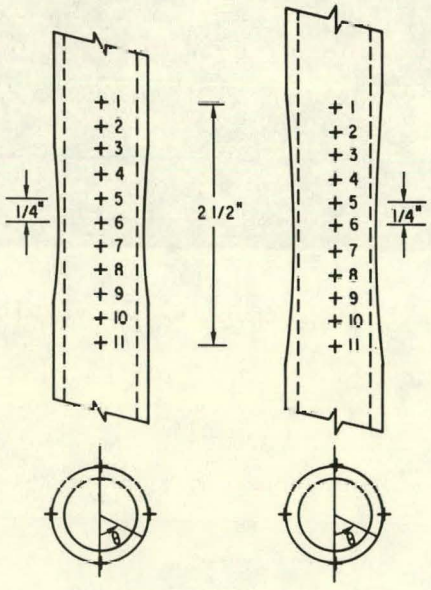

Fig. 5

Thermocouple Location.
ANL Neg. No. 306-79-118.

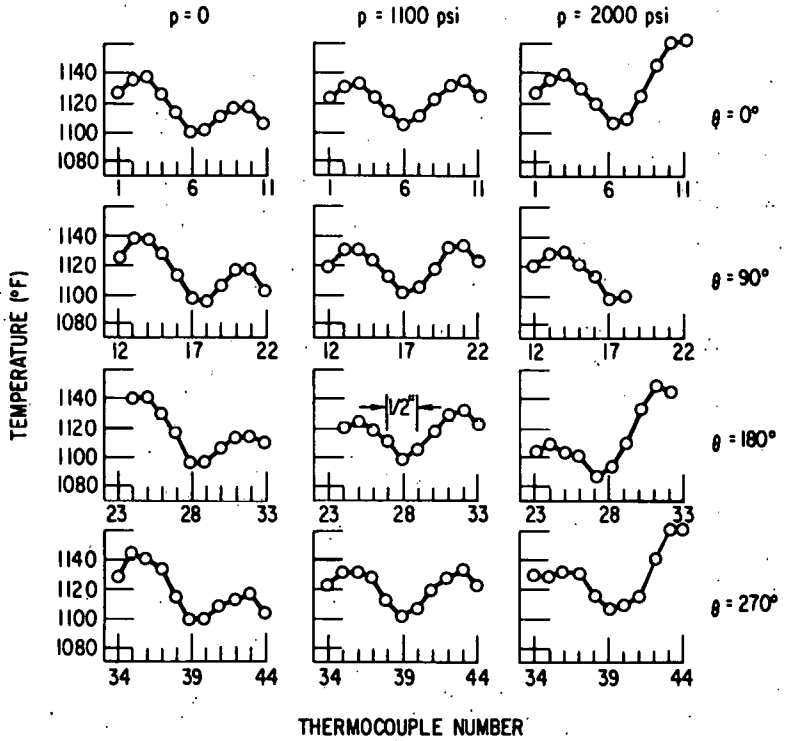

Fig. 6. Temperature Profiles in a Straight-gauge Specimen. ANL Neg. No. 306-79-120.

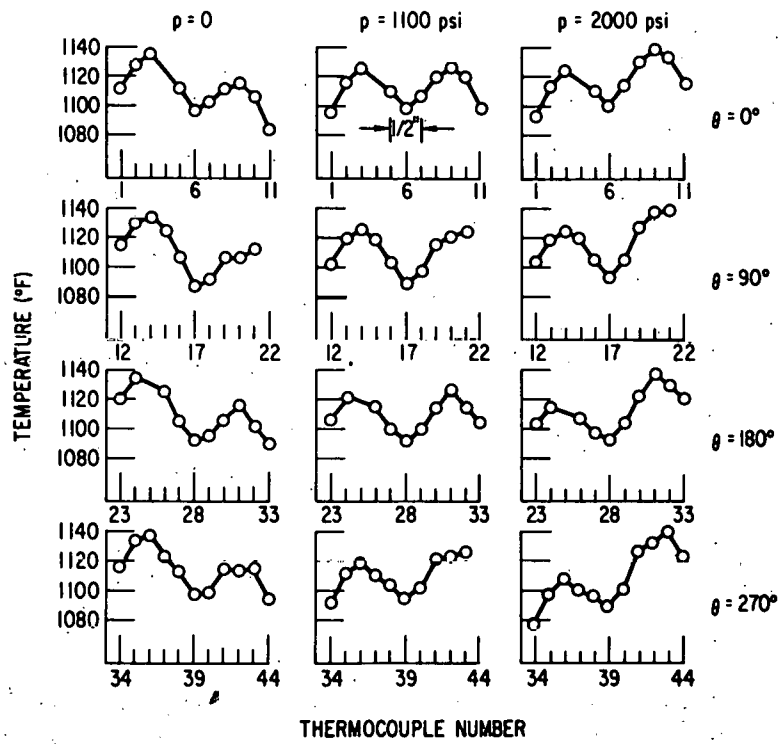

Fig. 7. Temperature Profiles in an Hourglass Specimen. ANL Neg. No. 306-79-116.

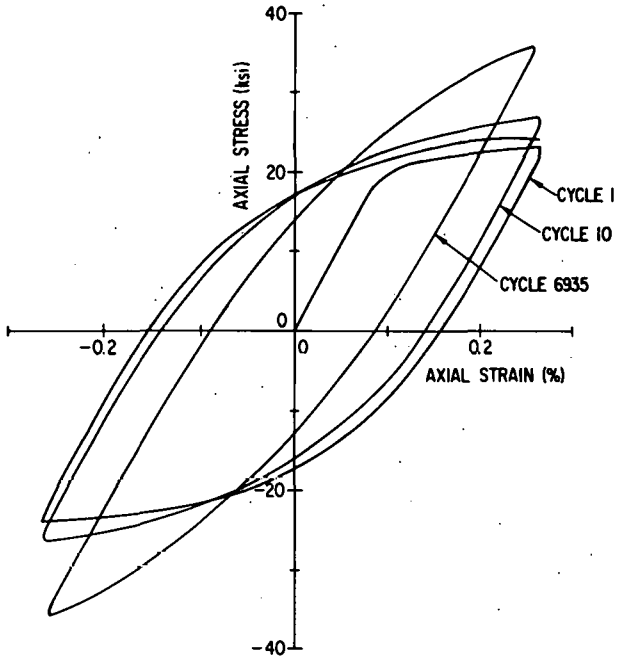

Fig. 8. Hysterisis Loops for Test No. 997. (p = 0, hold time = 0.) Neg. No. MSD-66261.

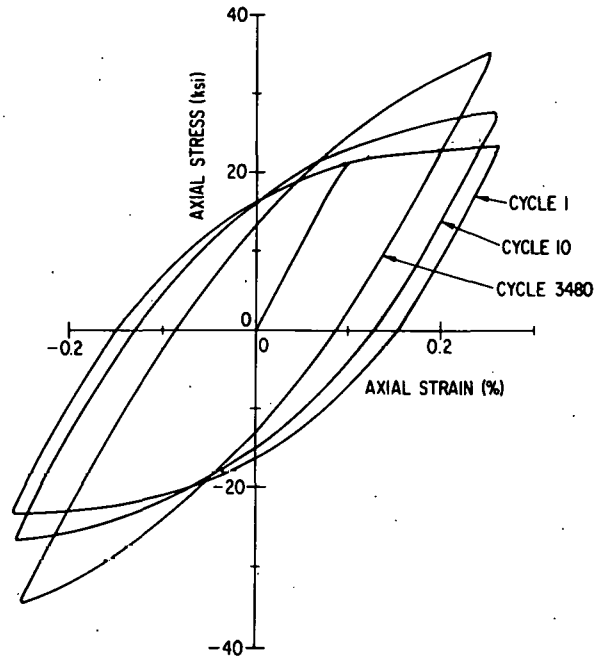

Fig. 9. Hysterisis Loops for Test No. 999. (p = 0, hold time = 0.) Neg. No. MSD-66241.

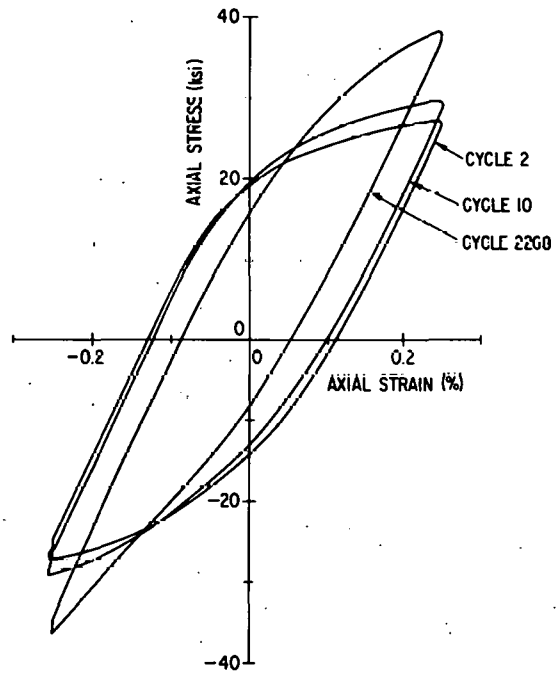

Fig. 10. Hysterisis Loops for Test No. 1027. (p = 0, hold time = 1C.) Neg. No. MSD-66247.

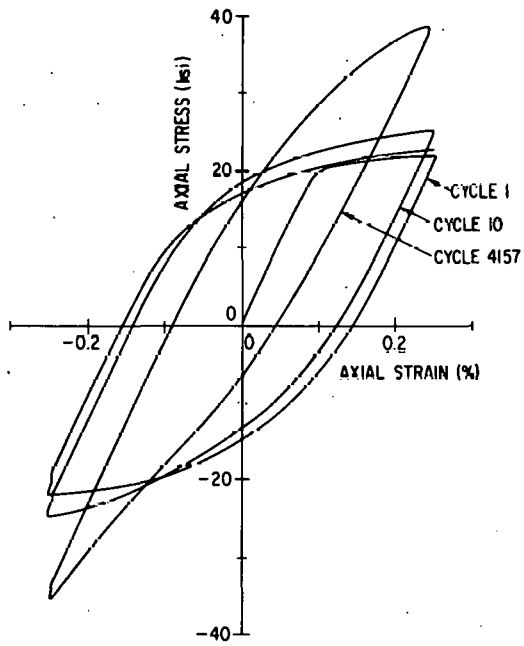

Fig. 11. Hysterisis Loops for Test No. 1035. (p = 0, hold time = 1C.) Neg. No. MSD-66248.

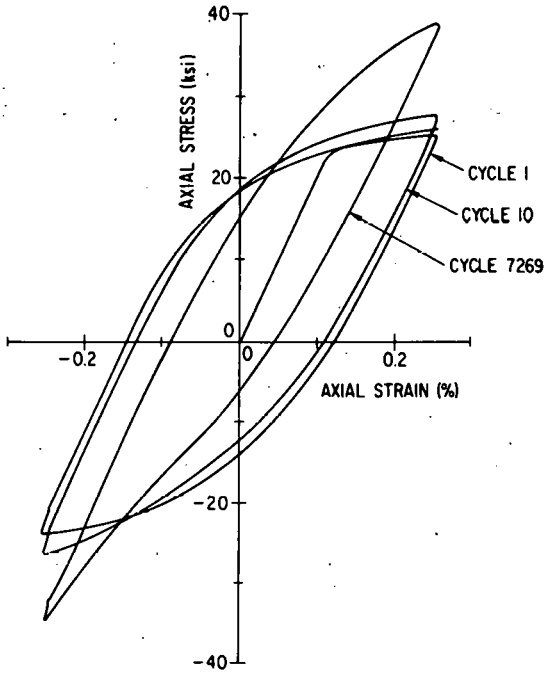

Fig. 12. Hysteresis Loops for Test No. 1052. (p = 0, hold time = 1C.) Neg. No. MSD-66252.

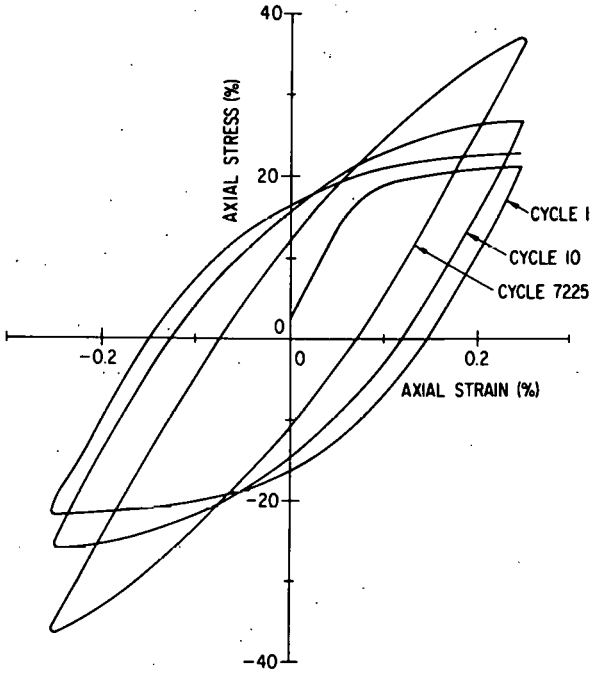

Fig. 13. Hysteresis Loops for Test No. 1001. (p = 1100 psi, hold time = 0.) Neg. No. MSD-66244.

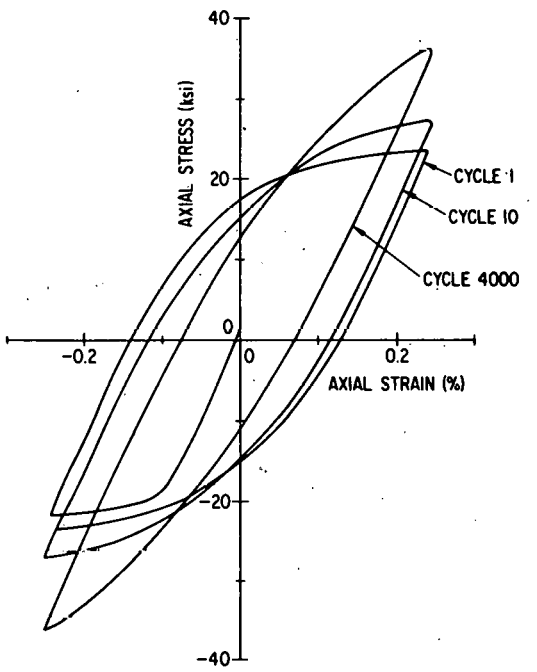

Fig. 14. Hysteresis Loops for Test No. 1012. (p = 1100 psi, hold time = 0.) Neg. No. MSD-66238.

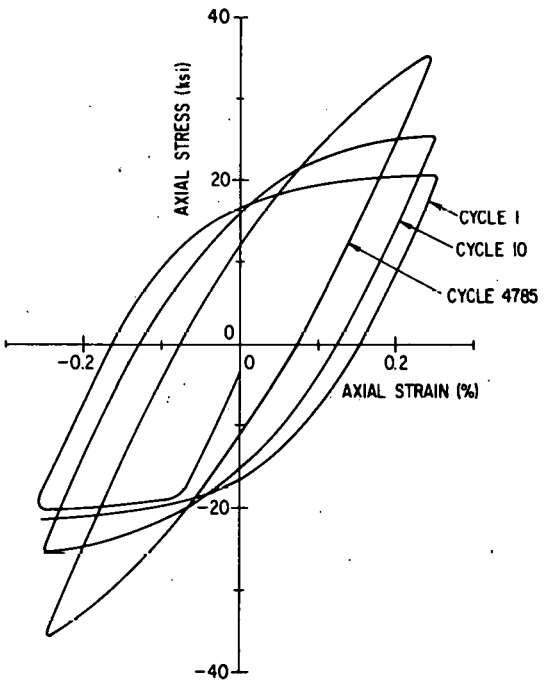

Fig. 15. Hysteresis Loops for Test No. 1044. (p = 1100 psi, hold time = 0.) Neg. No. MSD-66242.

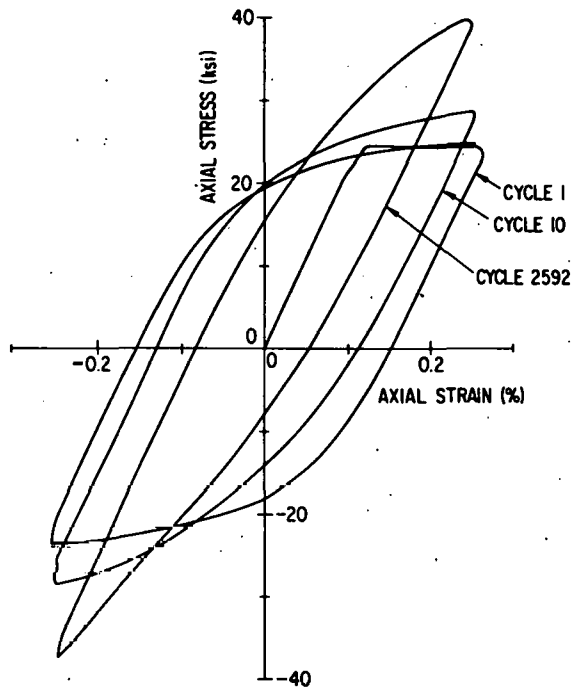

Fig. 16. Hysteresis Loops for Test No. 1024. (p = 1100 psi, hold time = 1C.) Neg. No. MSD-66259.

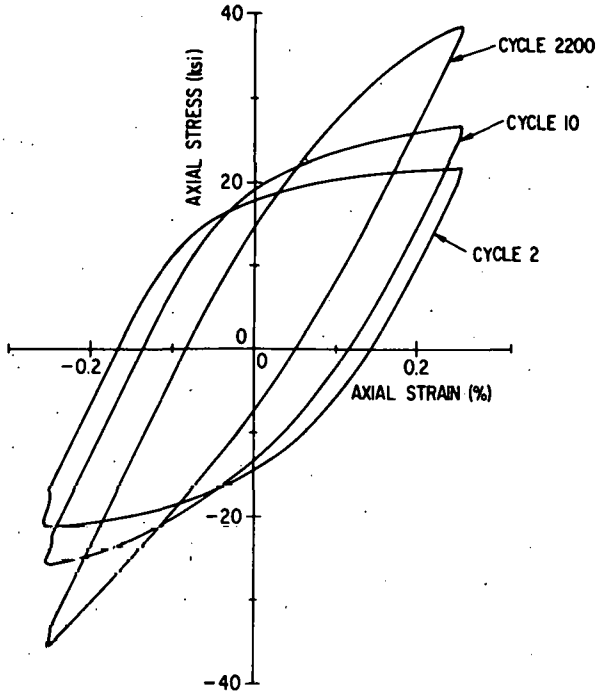

Fig. 17. Hysteresis Loops for Test No. 1033. (p = 1100 psi, hold time = 1C.) Neg. No. MSD-66251.

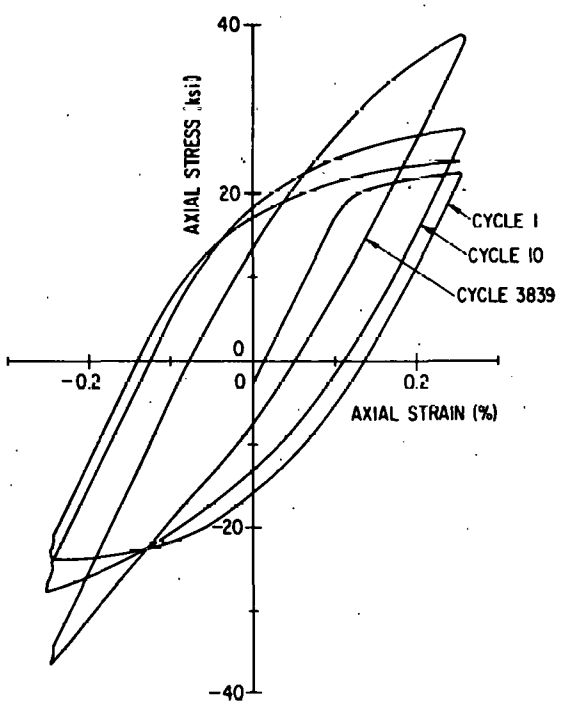

Fig. 18. Hysteresis Loops for Test No. 1049. (p = 1100 psi, hold time = 1T.) Neg. No. MSD-66257.

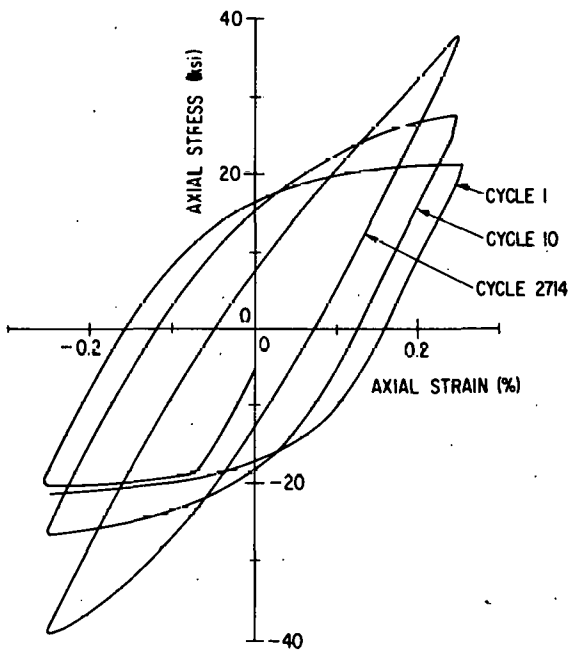

Fig. 19. Hysteresis Loops for Test No. 1038. (p = 1100 psi, hold time = 1T.) Neg. No. MSD-66245.

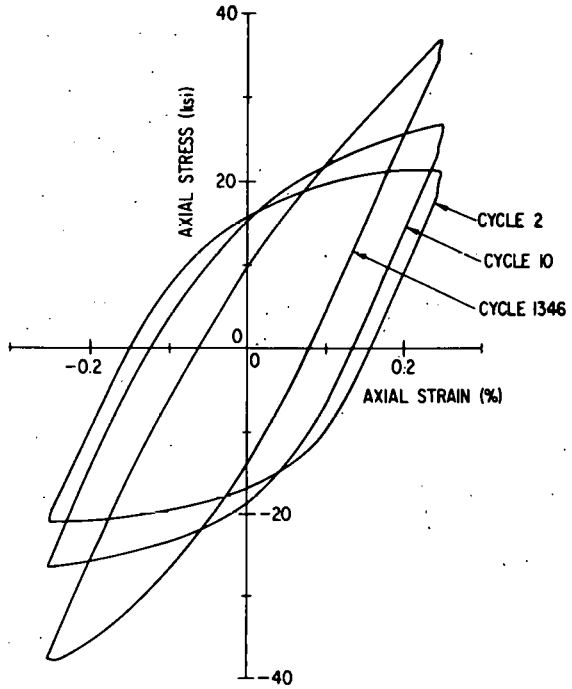

Fig. 20. Hysteresis Loops for Test No. 1041. (p = 1100 psi, hold time = 1T.) Neg. No. MSD-66260.

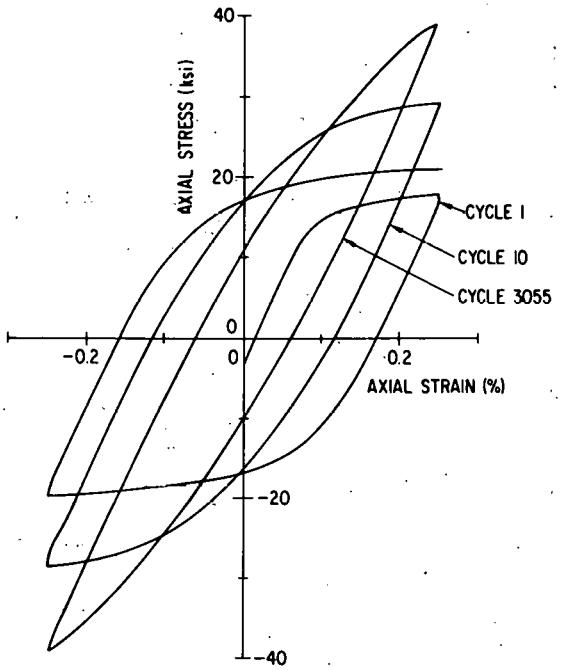

Fig. 21. Hysteresis Loops for Test No. 1031. (p = 2000 psi, hold time = 0.) Neg. No. MSD-66243.

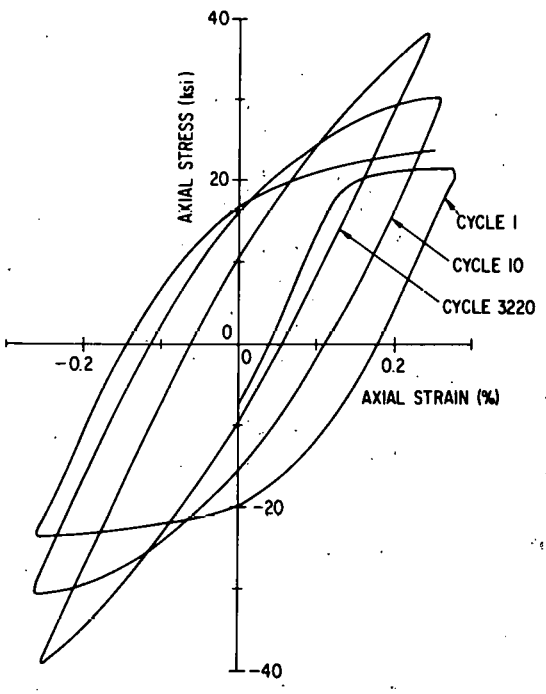

Fig. 22. Hysteresis Loops for Test No. 1059. (p = 2000 psi, hold time = 0.) Neg. No. MSD-66253.

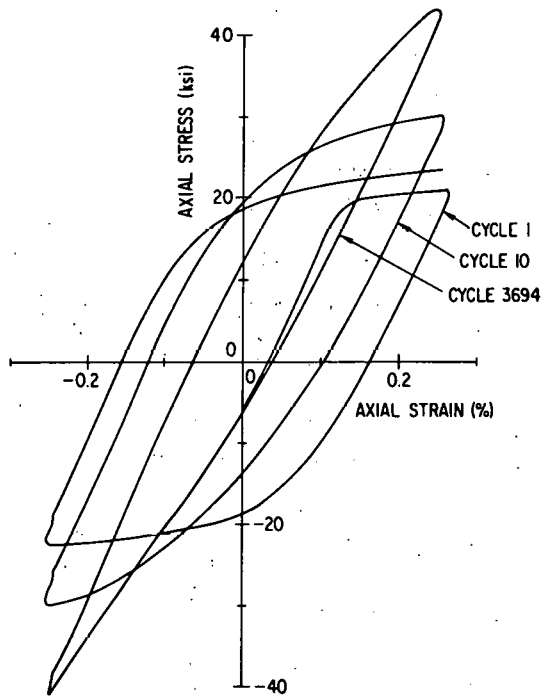

Fig. 23. Hysteresis Loops for Test No. 1050. (p = 2000 psi, hold time = 1C.) Neg. No. MSD-66246.

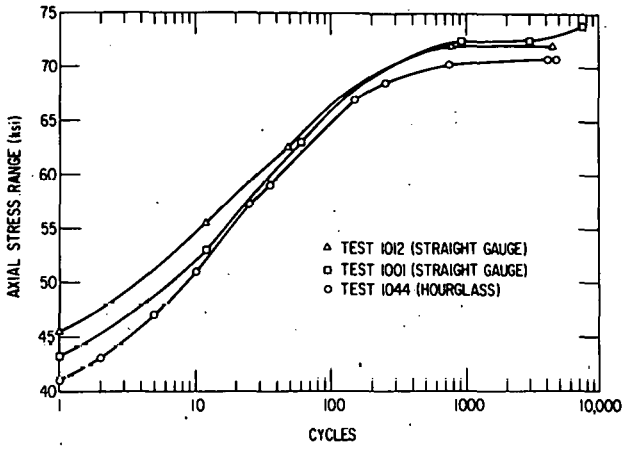

XXX

Fig. 24

Comparison of Axial Hardening Rate for Straight-gauge and Hourglass Specimens. Neg. No. MSD-66256.

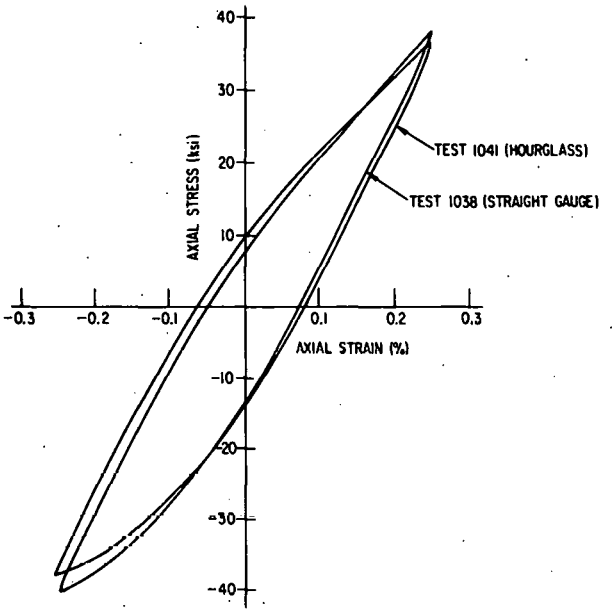

Fig. 25

Comparison of Hysteresis-loop Shapes for Straight-gauge and Hourglass Specimens. ANL Neg. No. 306-79-119.

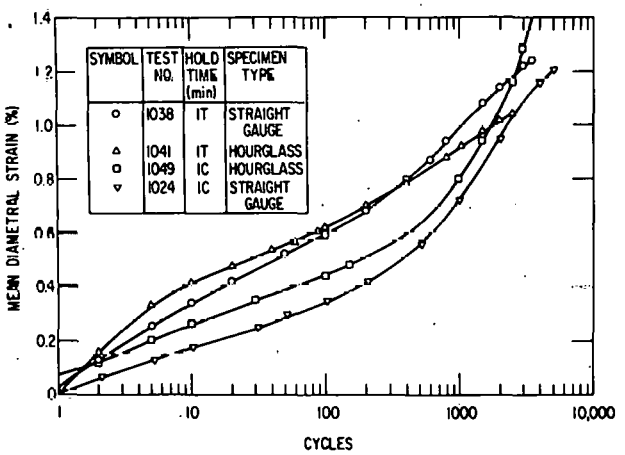

XX

Fig. 26

Comparison of Diametral Ratchetting Behavior of Straight-gauge and Hourglass Specimens. Neg. No. MSD-66249.

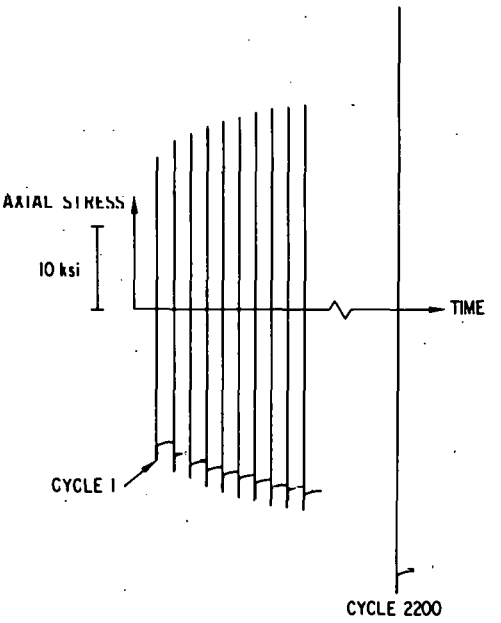

Fig. 27

Stress-relaxation Behavior for Test No. 1033. Neg. No. MSD-66239.

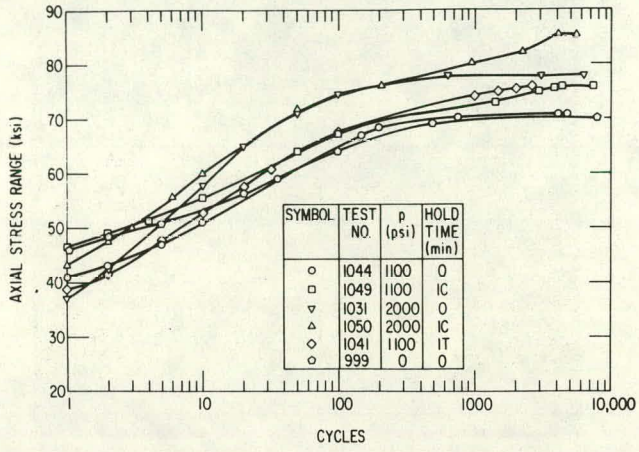

Fig. 28. Effect of Internal Pressure on Axial Stress-hardening Rate. Neg. No. MSD-66254.

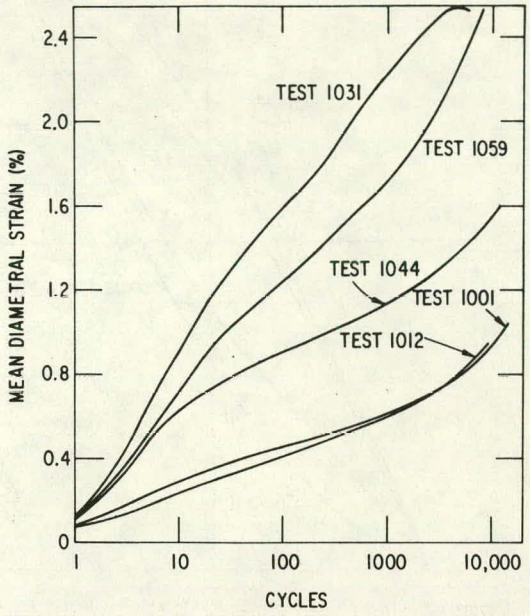

Fig. 29. Effect of Internal Pressure on the Diametral Ratchetting. Neg. No. MSD-66240.

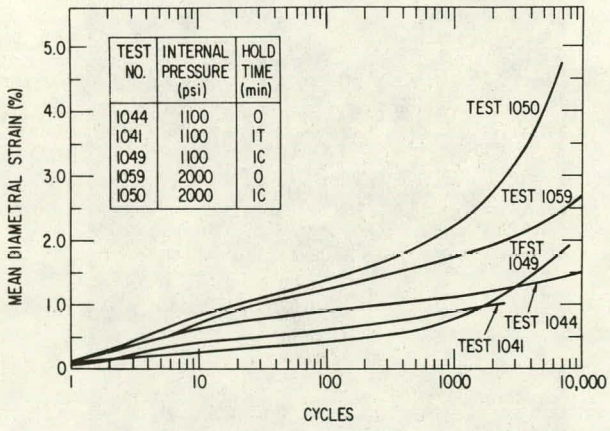

Fig. 30. Plots of Diametral Ratchetting vs Cycles. Neg. No. MSD-66250.

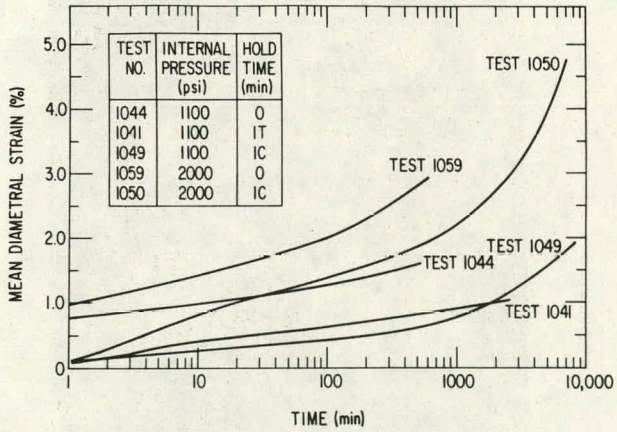

Fig. 31. Plots of Diametral Ratchetting vs Time. Neg. No. MSD-66255.

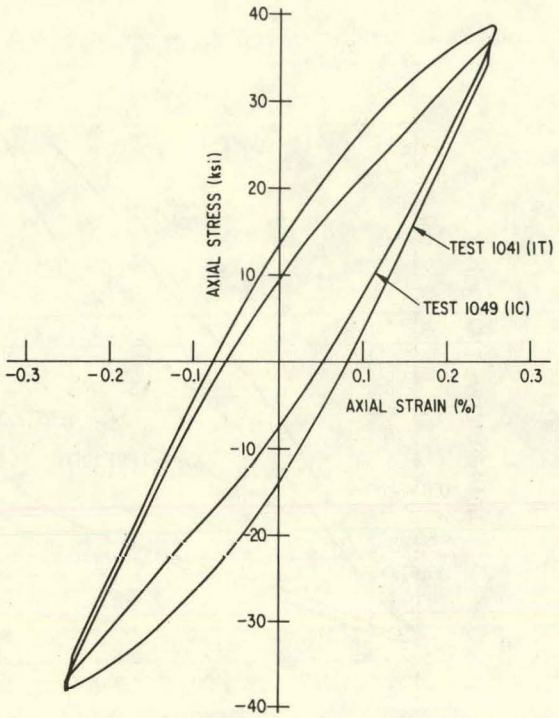

Fig. 32. Hysteresis Loops for 1-min Tensile and 1-min Compressive Hold-time Tests. ANL Neg. No. 306-79-121.

Fig. 33. Scanning Electron Micrograph of the Fractured Surface of Test No. 1044. Neg. No. MSD-66263.

Fig. 34. Scanning Electron Micrograph of the Fractured Surface of Test No. 1033. Neg. No. MSD-66262.

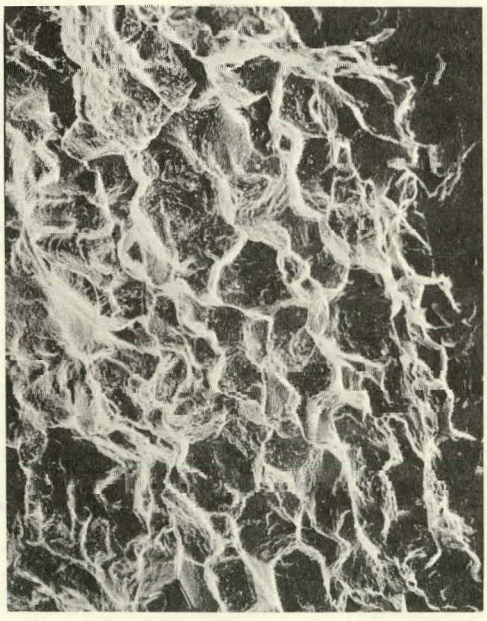

Fig. 35. Scanning Electron Micrograph of the Fractured Surface of Test No. 1041. Neg. No. MSD-66264.

Distribution for ANL-79-33

Internal:

B. R. T. Frost
J. J. Roberts
E. J. Croke
W. W. Schertz
S. Majumdar (20)
D. T. Raske
P. S. Maiya
W. J. Shack
W. Burke
D. Busch
M. Gorman
E. M. Stefanski (4)
A. A. Jonke
A. B. Krisciunas
ANL Contract File
ANL Libraries (5)
TIS Files (6)

External:

DOE-TIC, for distribution per UC-62c (296)
Manager, Chicago Operations and Regional Office, DOE
Chief, Office of Patent Counsel, DOE-CORO
President, Argonne Universities Association
Materials Science Division Review Committee:
- E. A. Aitken, General Electric Co., Sunnyvale
- G. S. Ansell, Rensselaer Polytechnic Inst.
- R. W. Balluffi, Massachusetts Inst. Technology
- R. J. Birgeneau, Massachusetts Inst. Technology
- S. L. Cooper, U. Wisconsin, Madison
- C. Laird, U. Pennsylvania
- M. T. Simnad, General Atomic
- C. T. Tomizuka, U. Arizona
- A. R. C. Westwood, Martin Marietta Labs.